2015-0548

Improved Methodology for Predicting the Force on Stalled Spinning Wings

Adam M. Ragheb* and Michael S. Selig†

University of Illinois at Urbana-Champaign, Department of Aerospace Engineering, Urbana, IL 61801

A novel analytical method is presented for the prediction of the normal force increment due to spin on a stalled wing. This model is based on the concept of fluid in the stalled semi-elliptical-shaped region behind the wing being pumped radially outward by centrifugal motion and ejected at the wingtip, where the ejection of flow at the tip is a new assumption. In the regime of $Re \approx 100,000$, the maximum normal force coefficient increment predicted in this investigation was approximately 1.4 based on the wing planform and aircraft pitch angle, θ. The analytical model was validated against wind tunnel tests conducted specifically as part of this research, where the relationship of C_N to ω^2 was confirmed. Good agreement was demonstrated between the presented model and full airplane rotary balance data for various wing planforms over the pitch range of $30 < \theta < 90$ deg and nondimensional spin parameter, ω, range $-0.9 < \omega < 0.9$. This method, which advances the current state of the field and leverages recent research from other fields, should provide useful results for wing modeling to provide a better design-for-spin, help improve the fidelity of transport category aircraft simulators for upset, loss of control situations or within the FAA "extended envelope," and aid in the simulations of flapping-wing aerodynamics for micro air vehicles or studies of insect flight.

Nomenclature

$\mathcal{AR}$	=	aspect ratio
b	=	wing span
c	=	wing chord
$\bar{c}$	=	wing mean aerodynamic chord
C_d	=	airfoil drag coefficient
C_D	=	drag coefficient
C_l	=	rolling moment coefficient
ΔC_l	=	change in rolling moment coefficient due to spin $[C_{l,\omega} - C_{l,\omega=0}]$
C_N	=	normal force coefficient
ΔC_N	=	change in normal force coefficient due to spin $[C_{N,\omega} - C_{N,\omega=0}]$
CG	=	center of gravity
$\dot{m}$	=	mass flow rate
q	=	dynamic pressure
R_g	=	radius of gyration
R_s	=	spin radius
Re	=	Reynolds number based on mean aerodynamic chord $[V\bar{c}/\nu]$
S_W	=	wing reference area
V	=	freestream velocity
x	=	aircraft longitudinal axis
$x_{c/4}$	=	x location of wing quarter chord
x_{CG}	=	x location of aircraft CG
x_{CP}	=	x location of wing center of pressure
y	=	aircraft lateral axis
Y_S	=	normalized wing spanwise location of stalled region $[2y_s/b_W]$
y_s	=	spanwise location of stalled region

*PhD Candidate, Department of Aerospace Engineering, 104 S. Wright St., AIAA Student Member.
†Associate Professor, Department of Aerospace Engineering, 104 S. Wright St., AIAA Associate Fellow.

z = aircraft vertical axis
α = angle of attack
$\alpha_{N,2}$ = end angle of attack for post-stall drag weighting function
$\alpha_{P,1}$ = beginning angle of attack for post-stall drag weighting function
λ = taper ratio
ρ = air density
θ = pitch angle
ω = spin parameter (positive for nose-right spin) [$\Omega b/2V$]
Ω = angular velocity about axis of spin (rad/s)

I. Introduction

The study of stall/spin aerodynamics for general aviation-sized aircraft continues to be an ongoing topic of interest.[1] There has been an interest in studying aircraft spin since the biplane era of the early 1930s[2] when the NACA studied how to improve the spin characteristics of the NB–1 seaplane trainer and the O2–E observation airplane through free-drop tests.[3] The free-drop method yielded too short of a timeframe for conducting satisfactory tests, and by 1932 researchers in England had constructed the first operational vertical spin tunnel with a 12 ft diameter[4] circular test section. The study of spin among general aviation (GA) sized aircraft is still very relevant, as accidents in which stall/spin are cited account for about 7% of total pilot-related single-engine accidents yet these accidents represent a staggering 65–70% of the total fatalities.[5] The only deadlier causal factor cited in accidents is weather, which is cited in only 5–6% of total pilot-related single-engine accidents but is a factor in 65–75% of the fatalities.

The stall/spin problem remains a technical frontier, and improvement of existing methods may have a significant positive impact on the industry, especially the general aviation market.[6] Stall/spin is a difficult problem due to the high angles of attack[7–9] and the associated highly-separated flow. In addition, any extrapolation from spin tunnel or radio-controlled (RC) model tests to full-scale vehicles is difficult because of Reynolds number effects.[10,11] A renewed interest exists in the field of loss-of-control events after the Colgan Air crash of 2009, and increased attention is being put on simulator manufacturers and airframers to accurately model airplane characteristics further beyond the normal flight envelope. On July 10, 2014, the FAA published a number of rulemaking documents, one of which proposed a mandate for an "extended envelope" to be incorporated into flight simulator training devices (FSTDs) within 5 years.[12] These devices are typically based off flight data, but in flight regimes where it is impractical and/or hazardous to obtain flight data, the FAA states that engineering predictive methods may be used to generate data. Such an engineering predictive method is presented here.

In 1981, a study was conducted by McCormick[13] that presented a mathematical model to predict the normal force (C_N) and rolling moment (C_l) coefficients on a spinning wing. A strip theory analysis was used in the study and the results of the model were compared to a single NASA rotary balance dataset.[14] The conclusion of McCormick's analysis was that the simple strip theory approach significantly underestimated the wing normal force and did not capture the dependency of spin rate on the normal force. It was suggested that this discrepancy was not because the 3D effects of the trailing vortex system (which would in fact reduce the predicted C_N) were not accounted for in the strip analysis, but that it was due to the presence of a "centrifugal pumping."[13] This centrifugal pumping was hypothesized to generate a spanwise pressure gradient in the separated flow behind the wing that moved with the wing as a solid body. The concept of the separated flow structures moving with the wing may have been provided by an earlier experimental study in which it was observed that the mechanisms of flow that generate the autorotative forces in a spinning wingless airplane-like configuration rotate along with the model and maintain their relative position.[15] On the subject of the spinning wing, it was hypothesized that no spanwise flow existed, as the pressure behind the stalled wingtip was presumed to be equal to that immediately outboard of the wing.[13]

Any study of the the stall/spin regime begins with the definition of the spin parameter, ω. The spin parameter is the standard nondimensional value that was adopted for describing spins, defined as[1,9,16–18]

$$\omega = \frac{\Omega b}{2V} \tag{1}$$

where b is the wing span, Ω is the angular velocity about the spin axis in rad/s, and V is the freestream velocity. The spin parameter is a measure of the flatness of a spin and is equal to the tip speed ratio,[19] a term commonly used in the study of wind turbines and boomerangs.[20] Low values of ω correspond to a steep spin with the aircraft pitched with

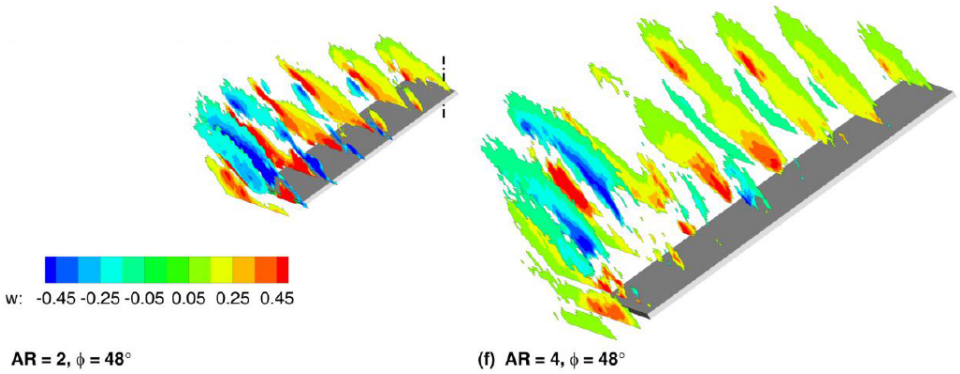

Figure 1. Plot of spanwise flow on rotating flat plate wings of $\mathcal{R} = 2$ and 4 at $\phi = 48$ deg (taken from Carr et al. [25]).

its nose toward the ground, while ω values above 0.9 correspond to a flatter spin mode where the nose is pointing in a nearly-horizontal direction.

The conclusions of McCormick,[13] the latter equation of which was corrected in a later paper by Pamadi and Taylor,[9,18] indicate that the corrections to C_N and C_l are given by

$$\Delta C_N = \frac{\omega^2}{3}(1+Y_S^3) \tag{2}$$

$$\Delta C_l = \frac{\omega^2}{16}(1-Y_S^4) \tag{3}$$

where Y_S is the normalized spanwise location ($2y/b_W$) outboard of which the wing is stalled. For the case of a fully-stalled wing, Eqs. 2 and 3 simplify to:

$$\Delta C_N = \frac{2\omega^2}{3} \tag{4}$$

$$\Delta C_l = 0 \tag{5}$$

A full-scale experimental investigation flown in Slingsby Firefly and Saab Safir airplanes used smoke and wool tufts on the wing upper surface to visualize a vortex located above the wing while in a spin.[21] The wing upper-surface vortex on the Firefly moved outward for the first two turns of a spin, drawing smoke towards the outboard section of the wing. From these observations, it was concluded that the tufts indicate spanwise flow in the outward direction exists on an aircraft wing in spin, and that the "centrifugal acceleration" acts in the spanwise direction, accelerating the air on the wing upper surface outward.[21] Some of the vortex visualization photographs appeared quite similar in structure to that of stall cells,[22–24] and the angle of attack regime in which the aircraft flew would initially have matched that in which stall cells have been observed.

A stereoscopic digital particle image velocimetry (stereo PIV) study of plates of $\mathcal{R} = 2$ and 4 at a tip $Re = 5,000$ provided insight into the size and structure of the spanwise flow behind a stalled spinning wing.[25] As seen in Fig. 1, a semi-elliptical region of radial flow exists behind a spinning flat plate wing, and as the flow moves outboard from the root to the tip, the region grows significantly in size. The experimental studies of Refs. 21 and 25 both indicate the presence of large vortical flow structures, and these vortex structures were observed to break down in the tip region after a yaw angle of more than 40 deg, where the flow became fully separated.[25] This fully-separated flow regime, in which the aircraft has yawed well beyond 40 deg from the onset of the spin and entered a developed spin, is the regime that the improved methodology presented in the present work models. While the stereo PIV study does not explicitly refer to the shape of the region of trapped flow as having an elliptical shape, it is clear from the images of Fig. 1 that the shape is indeed elliptical. Arie and Rouse[26] did specifically refer to the wake behind a nonrotating flat plate normal to a flow as being a closed region that was roughly elliptical in form and extended downstream approximately 2.4 chord lengths.

The objective of the present work is to propose a methodology for the prediction of the normal force due to a spin on a stalled wing, to validate the methodology with wind tunnel tests conducted specifically as part of this work, and demonstrate that the concepts behind the model are validated with the existing literature. Each step in the derivation

of and assumptions inherent to the described model are outlined as it is developed, and the validation of the proposed approach based on wind tunnel results specific to this research is presented. This proposed approach is then compared to historical data, and its improvement to the state of the field demonstrated.

II. Validation of Theory Behind Analytical Model

The theory and assumptions used in the development and derivation of this analytical model are supported by the existing literature. Both McCormick[13] and Clarkson[15] state that the the flow and forces rotate with the stalled wing, and it is noted that the presence of a centrifugal pumping effect creates a spanwise pressure gradient.[13] Where the method of the present model differs from the assumptions of McCormick[13] is in the radial ejection of fluid at the wingtip, which has been experimentally observed through PIV studies[25] as shown in Fig. 1. Complex vortical structures were initially observed near the wingtip, but after the stalled wing had yawed more than 40 deg, the complex vortex structures broke down and became entirely separated.[25] The concept of the flow moving with the wing and being ejected at the tip is therefore verified by the existing literature.

Figure 1, taken from Ref. 25, clearly shows the shape of the stalled, radially-flowing region to be that of a semi-ellipse, reasonably consistent from root to tip. This area of flow increases in size with spanwise location and similar results have been observed in the studies of Garmann[27,28] and others.[29] In Fig. 1, it is shown that as the flow moves radially outward, the size of the structure and the velocity both increase. Thus the scaling function that accounts for the entrainment of additional fluid beyond the 2D drag case is justified, for if no additional fluid were entrained, the increased cross-sectional area would result in the fluid slowing as it moves outward. In this case, the fluid is accelerated outboard both by centrifugal motion and the increase in the amount of fluid within the trapped wake. Figure 2, taken from Ref. 30, also shows that the region behind a stalled airfoil, in this case a thick wind turbine airfoil, is also similar to the assumed shape of Fig. 4(b). A significant fallout of the velocity and size of the stalled region growing towards the wingtip is the observation by McCormick that with both wings fully stalled, the radial pressure gradient should have no effect on the rolling moment.[13] The model presented in this study follows this observation, as the largest forces will be experienced at the wingtips due to the high velocity and $\dot{m}$ of the stalled region, and those forces will drive the total configuration C_l, thus masking any differences due to the local airfoil α and not affecting the rolling moment.

Comparing general aviation stall/spin to the field of wind turbines, both of which involve modeling rotating wings, Lindenburg[31] presented a model for the "rotational augmentation" that was first observed by Himmelskamp.[32] This augmentation results in wind turbines generating more power and thrust than predicted by 2D aerodynamic coefficients and is based on observations of a significant increase in the aerodynamic coefficients near the blade root and a reduction in those coefficients near the tip. The analytical method presented in this paper, however, predicts a significant increase in the aerodynamic coefficients near the tip. This increase in the aerodynamic coefficients near the tip is defendable because of the significant difference in the aspect ratio of general aircraft wings compared to horizontal axis wind turbine (HAWT) blades; general aviation wings have aspect ratios of around 6.5 while HAWT blades have values of around 20.[33,34] As a result, the Coriolis forces are more significant on wind turbines than in the case of a general aviation-style wing, and thus much of the radial flow exits at the trailing edge of a HAWT blade before it reaches the tip. Experimental data suggest that a maximum value of the ratio of wake length to the chord length of a bubble

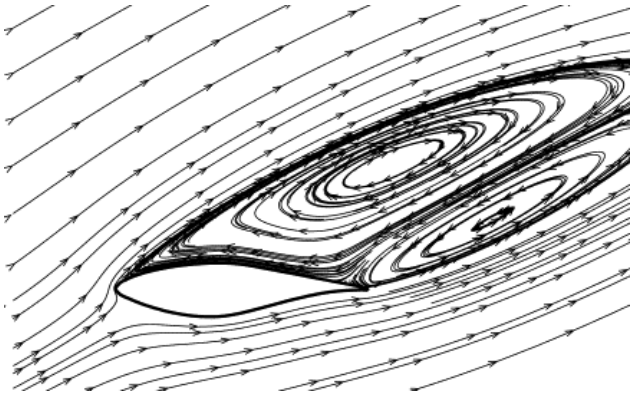

Figure 2. Plot of streamlines for a wind turbine airfoil at $\alpha \approx 25$ deg (taken from Hu et al. [30]).

behind a flat plate normal to a flow occurs for plates of $\mathcal{AR} \approx 10$.[35] The increased significance of coriolis forces and the resulting exit of radial flow via the blade trailing edge explains why a strong increase in the coefficients is observed at the root of a wind turbine blade, while for a general aviation wing, a large increase of the tip coefficients and a minimal effect on C_l is observed and predicted by this model. Further evidence of the significant differences between wind turbine blades and a spinning low-$\mathcal{AR}$ general aviation aircraft wing is given by Tangler and Selig,[36] who state that in the case of HAWTs, normal force increases would have the potential to greatly exceed 30%. Experimental spin datasets regularly demonstrate normal force increases on the order of 100%, which is significantly higher than those for wind turbines. Thus, it is defendable that this model for GA-type planforms predicts a large increase in the tip C_N due to spin, while the wind turbine literature observes coefficient increases at the root and coefficient decreases at the tip.

III. Analytical Model Development

A number of experiments, including the wind tunnel tests of this research, have verified that the normal force coefficient on stalled spinning wings is well in excess of the two-dimensional flat-plate drag coefficient of around 2.[37] Because of this, a stalled spinning wing cannot be analyzed based on two-dimensional aerodynamics alone, as significant three-dimensional effects, which account for the additional normal force, exist in such a situation. The methodology described here is used to generate a model for predicting those three-dimensional effects.

Viewing and analyzing the three-dimensional problem from a two-dimensional point of view, an increase in C_d beyond a value of 2 necessitates the removal of additional momentum from the flow when compared to the baseline two-dimensional case. Thus, a two-dimensional slice of a stalled spinning wing must "catch" more of the flow than it would in a standard, non-rotating, case. The most logical way to account for catching (i.e. entraining) the additional flow, and thus increasing the amount of momentum removed from a flow, is to introduce an additional sink downstream of the flat plate as depicted in Fig. 3. The entrainment of additional flow by the sink, and thus the removal of more momentum from the flow than in a non-rotating two-dimensional flat plate case, is what allows C_N to increase beyond the two-dimensional flat plate C_d value of 2.

Modeling the increase in the normal force coefficient C_N as the yaw rate Ω increases begins by defining the mass of fluid in the wake of the stalled wing. This fluid travels and rotates with the wing and is ejected at the wingtip after being accelerated by the rotational motion of the wing. This trapped flow is assumed to lie within a semi-ellipse with the area defined by

$$A_{ellipse} = \frac{\pi}{2} r_1 r_2 \tag{6}$$

where r_1 and r_2 are the semi-major and semi-minor axes, respectively. With a semi-major axis $r_1 = 3.25 c_{W,i}$ and a semi-minor axis $r_2 = c_{W,i}/2$, Eq. 6 becomes

$$A_{wake,i} = \frac{\pi}{2}(3.25 c_{W,i})(c_{W,i}/2) w(\alpha_i) \tag{7}$$

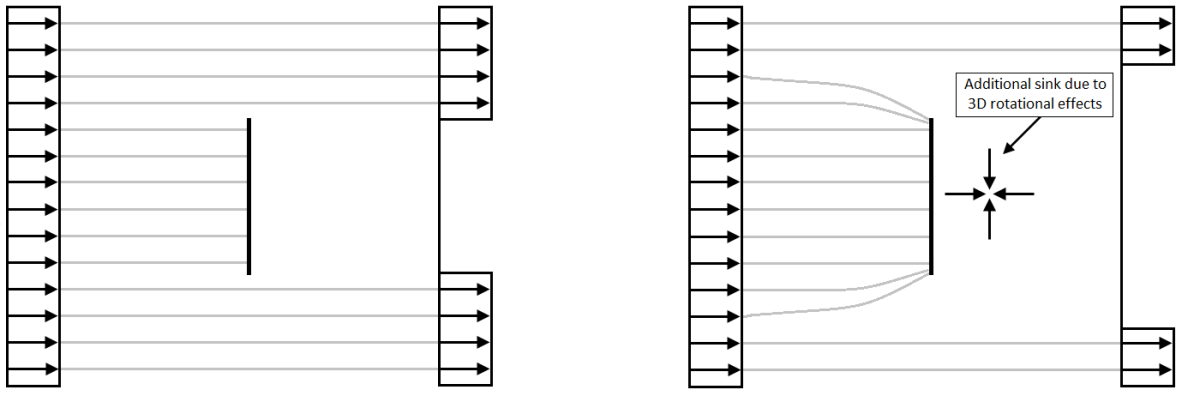

Figure 3. Illustration of a 2D flat plate (a) without and (b) with the influence of rotational effects present.

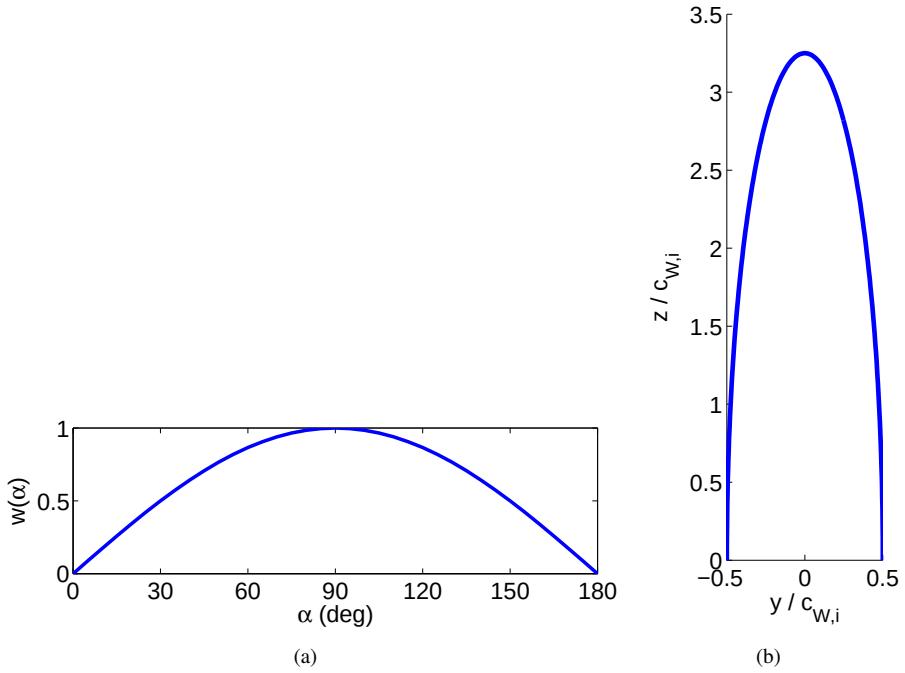

Figure 4. Plots of the a) scaling function used for ΔC_N in Eq. 8, and b) the semi-ellipse of trapped fluid behind a wing section with flow at $\alpha = 90$ deg, bottom to top.

where $c_{W,i}$ is the local wing chord at the i^{th} discretized wing section and $w(\alpha_i)$ is a weighting function that adds an α-dependency to the calculation. The selection of the relative size of the semi-major axis to the semi-minor axis is based off of the general dimensions of the elliptical wake as seen in Figs. 1–2, as well as the experimental measurements of Refs. 35 and 26. Figure 4(b) shows the dimensions of the unscaled semi-ellipse used in this methodology in terms of the local wing chord, $c_{W,i}$. The weighting function, $w(\alpha_i)$, is defined by

$$w(\alpha_i) = \sin(\alpha_i) \tag{8}$$

where α_i is the local angle of attack of the i^{th} wing slice and a plot of the weighting function is presented in Fig. 4(a). This weighting function is necessary because experimental data indicate a significant effect of varying the pitch angle, θ, of a spinning airplane. A variation in the local α across the wing would fall out from a variation in the aircraft pitch, θ. This weighting function is not limited to only the post-stall regime bounded by $\alpha_{P,1}$ and $\alpha_{N,2}$, the beginning and end α values that define the stall regime, as defined by Selig,[38] because even when the yawing wing is not stalled it is still reasonable to assume that some amount, albeit small, of spanwise flow due to rotational motion exists. In fact, spanwise flow was observed computationally on a spinning flat plate at $\alpha = 15$ deg.[28] Simplification of Eq. 7 yields

$$A_{wake,i} = \frac{13\pi}{16} c_{W,i}^2 w(\alpha_i) \tag{9}$$

Using $A_{wake,i}$, the mass of each individual slice of the wake is

$$m_{wake,i} = A_{wake,i} \rho \Delta y \tag{10}$$

where ρ is the density of the fluid and Δy is the thickness of each strip.

At this point in the derivation of the method, a simplifying assumption regarding the entrainment of additional fluid into the wake is introduced. While the literature suggests that Coriolis forces decrease the area of the wake as the radial location increases,[31] as discussed above, it is proposed here that additional fluid would be entrained along the span of the wing due to the lower pressure of the wing wake and the aforementioned three-dimensional sink effect of Fig. 3. In order to produce a reduced-form equation able to capture the first-order effects important for design,[36] the additional entrainment of fluid into the wake behind the wing is assumed to result in a linear increase in the original mass of each slice. This increase is modeled as a linear growth from 100% to 250% of the original mass of each slice

as predicted by Eq. 10 as one moves outward radially from the wing centerline ($y = b/2$) to the wingtips ($y = 0$ and $y = b$). Thus, the mass of the fluid in each wing slice becomes

$$m_{wake,scaled,i} = A_{wake,i}\rho S(y)\Delta y \tag{11}$$

where $S(y)$ is a linear scaling function with the points $(y, S(y)) = (0, 2.5)$, $(b/2, 1)$, and $(b, 2.5)$ that accounts for the entrainment of additional flow into the trapped stalled wake downstream of the stalled wing due to the local angular velocity. The reason that $S(y) = 1$ at the wing centerline is because the angular velocity of the wing section is 0 at that point because $r = 0$ at the center of rotation. The acceleration of the fluid inside each slice, i, due to rotation is defined by

$$a_i = \Omega^2 y \tag{12}$$

where Ω is the yaw rate and y is the radial location from the wing centerline of $y = b/2$. It is the established theory of sources and sinks that specifies the amount of fluid in the stalled wake as the radial location moves outboard, since additional fluid is being entrained. Newtonian physics yields:

$$\Delta F_{spin} = m_{wake,scaled,i} a_i \tag{13}$$

for each individual wing slice. Summing up the forces across the entire wingspan, ΔC_N can be calculated by

$$\Delta C_N = \sum_{i=0}^{b} \frac{13\pi\rho\Omega^2}{16} c_{W,i}^2 w(\alpha_i) S(y) y \Delta y \tag{14}$$

where $c_{W,i}$ is the local wing chord, $w(\alpha)$ is the scaling function of Eq. 8, $S(y)$ is the linear-scaling function from before, and y is the radial distance from the wing semispan of each slice of width Δy.

This correction due to spin does have an effect on the pitching moment and the magnitude of the change in pitching moment due to the additional ΔC_N is given by

$$\Delta C_m = \Delta C_N (x_{CG} - x_{c/4}) \tag{15}$$

where ΔC_N is defined by Eq. 14, and x_{CG} and $x_{c/4}$ are the centerline locations of the CG and wing quarter chord, respectively.

The final correction due to spin consists of an antispin yaw moment caused by the work required to provide the radially-pumped fluid with its rotational velocity. This correction is based off the classic undergraduate fluids "sprinkler problem," where the task is to determine the rotational velocity of a frictionless lawn sprinkler given the fluid mass flow rate and the angle at which the fluid is ejected at the tip. Adapted to the field of stall/spin, the problem becomes one where given a specified rotational rate and mass flow rate, how may the torque required to radially accelerate the volume of fluid within the wing wake (i.e. a maintaining torque) be calculated. This maintaining torque would be manifested in a developed stall/spin situation as an antispin yaw moment, but would not be a main driver of the yaw moment; the side force from the fuselage and vertical tail would be the drivers of the yaw moment. For a one-dimensional, non-deformable control volume, and based off the parameters of Fig. 5. It can be shown that:

$$\int_{CS} (\mathbf{r} \times \mathbf{V})\rho(\mathbf{V} \cdot \mathbf{n}) dA \approx \sum M_O = T_O = \sum (\mathbf{r} \times \mathbf{V})_{out} \dot{m}_{out} - \sum (\mathbf{r} \times \mathbf{V})_{in} \dot{m}_{in} \tag{16}$$

Because the force acts radially through point O, the final term drops out, and the equation for the torque required to maintain the angular rate of ω, T_o simplifies to

$$T_o = (\bar{r}_E \times \bar{V}_E)\dot{m}_E - (\bar{r}_o \times \bar{V}_o)\dot{m}_o \tag{17}$$

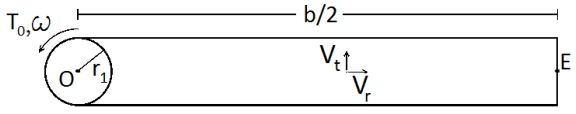

Figure 5. Illustration of the classic sprinkler problem adapted for this research.

Using Eq. 11, the relationship between $\dot{m}_E$ and $\dot{m}_o$, the mass flow rates at the wingtip and wing root, respectively, may be defined as

$$\dot{m}_E = \frac{S(b)}{S(b/2)}\dot{m}_o \tag{18}$$

Applying the cross product to Eq. 17, noting that $V = \omega r$ and $r_E = b/2$, and taking the radius of the fluid source to be r_1 yields the final expression for the maintaining torque, which is manifested as ΔC_n

$$\Delta C_n = \dot{m}_o \omega \left(\frac{S(b)}{S(b/2)} [b/2]^2 - r_1 \right)^2 \tag{19}$$

It should be noted that this contribution to the yawing moment coefficient is small and does not drive the aircraft yawing moment. The change in aircraft C_n in a spin is primarily driven by the fuselage cross-sectional shape, and the effectiveness and level of flow shielding presented by the horizontal stabilizer on the vertical stabilizer when in a spinning situation.

IV. Experimental Methods

Aerodynamic tests of spinning wings were conducted in the UIUC low-turbulence subsonic wind tunnel in order to validate the aforementioned computational model for 3D forces on a stalled spinning wing. The wind tunnel is of the open-return type and has a contraction ratio of 7.5:1. The test section is rectangular and has a cross-section of 2.8×4.0 ft (0.853×1.22 m) and is 8 ft (2.44 m) in length. Over the length of the test section, the width increases by approximately 0.5 in (1.27 cm) to account for the growth of the boundary layer at the test section sidewall. Four anti-turbulence screens and one 4-in (10.2-cm) honeycomb screen are located in the settling chamber to ensure low levels of turbulence in the test section. The result due to these screens is an empty-tunnel turbulence intensity that has been measured to be less than 0.1% for all operating conditions.[39,40] The maximum empty-test-section speed is 235 ft/s (71.5 m/s), but the tunnel was not operated above 30 ft/s (9.1 m/s) in the current research; a 125-hp (93.2-kW) AC motor driving a five-bladed fan is used to control the test-section speed. Test section speed was computer-controlled to within 1% of the prescribed speed. The test-section speeds were measured with an MKS 220 1-torr differential pressure transducer connected to static ports in the settling chamber and at the beginning of the test section. Ambient pressure was measured with a Setra Model 270 pressure transducer and the ambient temperature was measured with an Omega GTMQSS thermocouple.

The normal force was measured through the use of a drag balance that pivoted on two sealed ball bearings and was constrained on the downstream side by a load cell.[41] The propeller rig of Ref. 42 was modified, replacing flexures with ball bearings and reversing the streamwise orientation of the load cell in order to account for the higher loads and measurement of drag instead of thrust, respectively. An Interface SMT S-type load cell with a load capacity of 10 lb (44 N) was used. Ten different locations, ranging from 3.25 in (8.26 cm) to 7.75 in (19.69 cm) from the pivot point in 0.5-in (1.27-cm) increments, were available for locating the load cell in order to utilize the full measurement range of the load cell at varying drag values. The weight and resulting moment of the motor and sting structure was more than sufficient to maintain the load cell in tension for all test cases, thus ensuring that the load cell was prevented from slipping in a negative drag condition. A fairing utilizing an NACA 0025 airfoil of chord length 24 in (0.61 m) was used to keep the torque cell, motor sting, balance support arm, and cabling out of the wing wake and test section. This fairing, depicted in the experimental setup photograph of Fig. 6, spanned the entire test section from the floor to the ceiling in order to maintain a symmetric test section. The motor sting, which placed the rotating wings 17.5 in forward of the fairing leading edge, was of a sufficient length to ensure all rotating wings were more than 7.75 chord lengths (or at least 1.7 diameters) upstream of the fairing in order to minimize the fairing's effect on the wake structure behind and resulting drag of the spinning wing.[42]

The wings were spun by a Faulhaber 3268G024BX4AES-4096 brushless DC-servomotor which was controlled by an MCBL 3006 AES-series motion controller connected via an RS232 cable to a computer running the Faulhaber Motion Manager 5.1 software. This software allowed for the motor rotational speed to be set to and maintained at specific RPM values and monitored in real time. The 3268 series DC-servomotor has an operating range of 0 to 11,000 RPM and is capable of a maximum torque of 92 mNm at 2.59 A. Absolute shaft position information is provided by the absolute encoder of the motor to the motion controller at a resolution of 4096 steps per revolution via a serial (SSI) interface. Proper power was supplied to the DC-servomotor by an NEC NG-150642-001 24-V 600-mA power supply that was connected to the motion controller, which subsequently supplied the motor with power.

All of the testing instrumentation voltages were channeled to and recorded by a National Instruments PCI-6031E 16-bit analog-to-digital data acquisition (DAQ) board that was connected to a personal computer. The DAQ board can

Figure 6. Experimental setup of spinning wing mounted forward of sting and support arm fairing.

Table 1. Wing Blade Information and Dimensions

Aspect Ratio	Raw Blade	Chord Length (in/cm)	Wingspan (in/cm)	Area (in^2/cm^2)
8.33	Align 325D 325 mm	1.25 / 3.2	10.4 / 26.4	13.01 / 83.9
6.50	KBDD 32W 325 mm	1.37 / 3.5	8.91 / 22.6	12.21 / 78.8
4.85	Revolution RVOB043000 430 mm	1.65 / 4.2	8.00 / 20.3	13.20 / 85.2
3.85	KBDD 350W 350 mm	1.85 / 4.7	7.13 / 18.1	13.19 / 85.1
2.55	Pro3D DY-6001 600 mm	2.20 / 5.6	5.61 / 14.2	12.34 / 79.6

simultaneously recieve up to 32 differential analog inputs at a sampling rate of up to 100,000 Hz. The spinning wing RPM was set and controlled by the Faulhaber Motion Manager 5.1 software and was operated from a separate laptop computer. A LabVIEW program was modifed to simultaneously record the drag, dynamic pressure, atmospheric pressure, and temperature at 3,000 Hz for a duration of 3 sec. These 9,000 points were then averaged to create a single data point, and three separate data points were acquired at each motor RPM setting. Each wind tunnel run was at a constant speed, and the RPM was varied to produce the desired range of ω values. The LabVIEW program also controlled the wind tunnel speed and received the set motor RPM in order to calculate the spin parameter values. Selected time histories of the DAQ board data and motor RPM values were recorded, and the differences in motor RPM values were observed to change less than 1% during the recording time period.

The spinning wing test articles were made using a 3/16 in (4.76 mm) diameter steel shaft and symmetric RC helicopter blades of varying chord lengths and approximately a 10% t/c ratio. The test articles were linked to the 5 mm shaft of the motor with a KBK KB2/15-26-0.1875in-5mm bellows coupling that was replaced approximately halfway through the testing with a Ruland MBC15-5mm-3/16in bellows coupling. Holes were drilled at 90, 60, and 30 deg orientations to the shaft, and the shaft was epoxied into the hole so that its tip was reasonably flush with the forward-facing surface of the blade. The dimensions and information for the five blades are summarized in Table 1, which presents the $\mathcal{AR}$, chord length, wingspan, and area of each of the five wings. The area of each wing was held as close as practicable to 13 in^2 (84 cm^2) and resulted in a range of $\mathcal{AR}$ values that included and expanded beyond values that would be seen on typical GA aircraft.

After each test article was assembled, it was statically balanced along the span. This was achieved through a combination of removing any counterweights from inside the blade and gluing small steel bolts into the foam core at the wingtip. A finer level of balancing was then achieved by adding drops of epoxy to either the wingtip or to the wingtip center upper surface while balancing the blade on its shaft on the edge of a table. Once the blade would settle

level with the table surface, it was considered to be balanced. On the 90 deg blades, the holes were located at the 50% chord location because that is where the force was expected to act in the heavily stalled situation (as opposed to the 25% chord location for an unstalled airfoil). For the 30 and 60 deg blades, the shaft was located as close as possible to passing through the 50% chordline despite the fact that structural considerations had to be the primary driver of hole location.

V. Experimental Results

For this research, wings of five different aspect ratio values were tested at three different pitch angles. Time-averaged data for the wing normal force was acquired over the approximate range of $-1 < \omega < 1$. The first experimental step was to determine a Reynolds number at which to test the spinning wings. The limiting factor in this experiment was the RPM value below which no significant vibrations were observed. The limiting rotational speed for these wings was determined to be approximately $\pm$400 RPM. After that value was determined, a wind tunnel velocity was selected so that experiments would cover a sufficient range of values of the spin parameter ω. After determining that no Reynolds number effects were present, the wings were tested at a Reynolds number of 11,000 based on the wing chord. This Reynolds number corresponded to wind tunnel velocities of between 9.2 and 16.5 ft/s.

Figure 7 presents C_N versus ω plots for the five different aspect ratio wings at $Re = 11,000$, clearly showing that C_N is proportional to ω^2 and that the effects of aspect ratio are much more pronounced at 30 deg than at 90 deg. Figure 7 (a) is at $\theta = 30$ deg, (b) is at $\theta = 60$ deg, and (c) is at $\theta = 90$ deg. In Fig. 7(a), the differences between the five aspect ratio wings are evident, as distinct curves are visible. As one moves from the $\theta = 30$ deg case of Fig. 7(a) to the $\theta = 60$ deg case of Fig. 7(b), and the $\theta = 90$ case of Fig. 7(c), the curves exhibit higher values of C_N for a given value of ω. The lower aspect ratio wing data exhibit a greater C_N value for a given value of ω as θ increases than the higher aspect ratio wing data, implying that the effects of θ on C_N increase for lower aspect ratio wings. It is possible that the flow mechanisms behind lower $\mathcal{AR}$ wings at low, but poststall, θ values are characterized by strong downwash over much of the wing due to the influence of the tip vortices. As the span increases, but still at low θ values, the influence of the tip vortices is restricted to a smaller region of the wing, and thus the normal force produced by the higher aspect ratio (and span) wing is larger. This influence of the tip vortices is more prevalent at low values of θ because the wing, while stalled, is closer to an unstalled, flying state. As θ increases to 60 deg, the wing is now behaving much closer to a flow-normal flat plate, with less turning of the flow present and the subsequent reduction in any tip vortex-like structures. At $\theta = 90$ deg, no turning of the flow is present, and thus no tip vortices are present. With no tip vortices present, the aspect ratio (and span) differences have a significantly reduced effect for this range of aspect ratio values, and thus the C_N curves lie nearly atop one another.

The C_N values for the $\mathcal{AR} = 2.55$ and 3.85 wings grow significantly more rapidly with ω than the higher aspect ratio wings in the regime $-0.5 < \omega < 0.5$. The authors propose that this is due to the centrifugal pumping in that regime pushing any wingtip vortices outboard which significantly reduces the downwash induced on the wing, thus allowing the C_N value to grow more rapidly and close the gap to the higher aspect ratio wings. For the $|\omega| > 0.5$ regime, it appears that this effect has reached its limit, as all of the C_N curves grow at approximately the same rate, with a much smaller vertical offset than in the $|\omega| < 0.5$ regime.

VI. Modeling Results

In this section, the analytical model described in Section III is added to a strip-theory-based force calculator and is used to simulate the forces on a full-airplane configuration for which experimental data are available. Full airplane forces were calculated using a component-buildup method[38] where the aircraft was divided into four components: the wing, the fuselage, the horizontal tail, and the vertical tail. The horizontal and vertical tails were each treated as single elements, while the wing and fuselage were each discretized into segments. Aerodynamic lookup tables were generated for each of the two tail surfaces, as well as for the wing airfoil and approximated fuselage cross-section. The data demonstrate that wings with different planforms (namely different values of the taper ratio λ) exhibit different growth rates with respect to ω, and that the current model is able to capture those different growth rates.

The results of adding Eq. 14 to a strip-theory-based force simulator of a spinning airplane are presented in Fig. 8(a) and those results are compared to the experimental data of Ref. 43. The wing planform had an $\mathcal{AR} = 7.24$, $\lambda = 0.67$, and the configuration of the aircraft resembled that of a generic low-wing, single engine GA aircraft such as the Piper Warrior. As visible in Fig. 8(a), good agreement between the analytical model and experimental results is obtained, especially at higher values of θ. At $\omega = -0.9$, the predicted C_N values are almost identical to the experimental values for $\theta = 55$, 70, and 90 deg. While the analytical curves are symmetric about the y-axis, some variation is observed

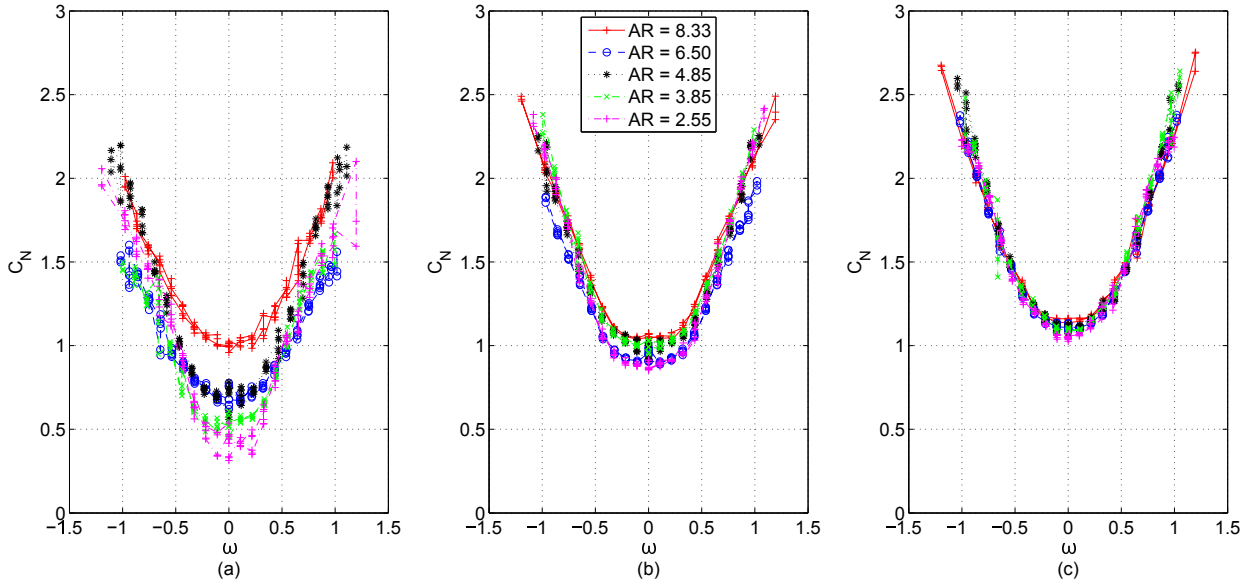

Figure 7. Plot of ω versus C_N for five different $\mathcal{AR}$ values at $Re = 11{,}000$ at a) $\theta = 30$ deg, b) $\theta = 60$ deg, and c) $\theta = 90$ deg.

in the curves of the experimental data. An effect, where C_N grows, then decreases, then grows again, is evident in the results. In the case of Fig. 8(a), this effect is characterized by a slight increase in analytical results for C_N from $\omega = 0$ until $|\omega| = 0.1$, then a decrease through $|\omega| = 0.2$, and then an increase over the remaining range of ω. This effect is solely an artifact of the strip theory aspect of the force calculation, as when the total calculated normal force was broken down into its standard strip theory and additional rotational forces, only the former exhibited the effect. This growing-decreasing-growing effect was also observed to some degree in the experimental results, and in the case of Fig. 8(a), it is somewhat more prominent at $\theta = 80$, 70, and 60 deg for values of $|\omega| \leq 0.2$. The analytical C_N curve appears to grow too rapidly with an increase in the magnitude of ω for a θ value of 30 deg, but, once again, this is an artifact of the strip theory calculations, as it was the strip theory portion of the model that predicted certain portions of the wing to be right at or below stall, and did not account for the spanwise flow in those regions that would significantly degrade the lift performance of the wingtip sections.

The analytical method of this paper was also validated against a simpler wing with $\lambda = 1.0$ and $\mathcal{AR} = 5.9$, and a comparison of the analytically predicted and experimentally measured C_N values are presented in Fig. 8(b). The same general features of Fig. 8(a) are present in Fig. 8(b). The growing-decreasing-growing effect is present in the rotary balance datasets at θ values of 90, 80, and 70 deg and $|\omega| \leq 0.2$. While a good fit to the growth rate is observed at high values of θ, the analytical predictions at $\theta = 30$ deg grow more rapidly than the experimental data. Once again, this effect is not an artifact of the spin correction to C_N of Eq. 14, but an artifact of the strip-theory-based calculations, as mentioned earlier, which are not the subject of this paper.

When comparing Figs. 8(a) and 8(b), it may be observed that the C_N values in general grow at a much higher rate in the latter figure, creating a taller and narrower parabola shape. This increased growth rate as a function of ω is due to differences in the aircraft wing planform, namely the taper ratio, λ. The regions of the wing experiencing the highest local velocity are of course located farthest outboard, and in the case of the tapered wing of Fig. 8(a), outboard regions of the wing have smaller chords, and thus produce a smaller magnitude of lift. As λ increases towards 1 (unity), those sections contribute a larger amount to the total C_N, and thus the parabola-like C_N vs. ω curve will grow at a more rapid rate as λ approaches unity. A similar effect of an increased rate of growth is also observed for a decreasing $\mathcal{AR}$ value.

VII. Comparison with Current Literature

The methodology of this paper was used to predict the increase in the normal force coefficient for rotary balance data acquired over the range of $30 < \alpha < 90$ deg and spin parameter values of $-0.9 < \omega < 0.9$. These predicted values were then compared against those predicted by the method of Eq. 4,[13] and the root mean square (RMS) error was calculated by

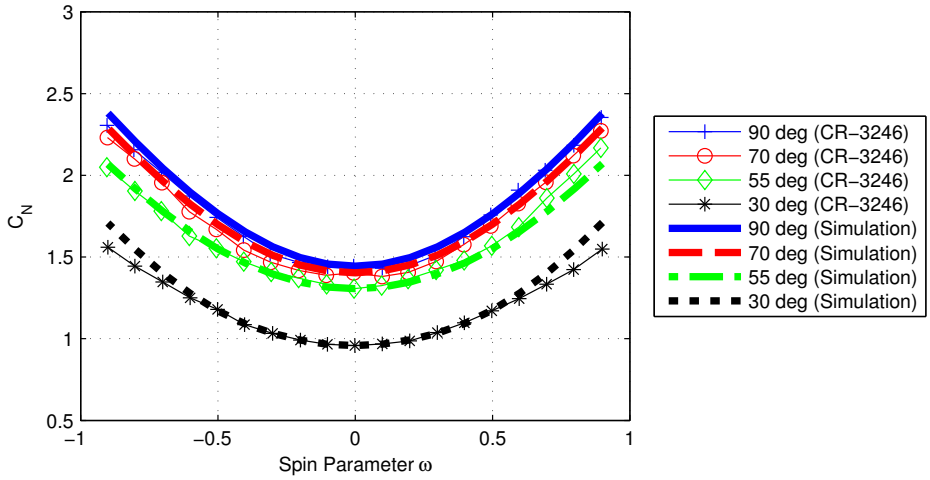

(a)

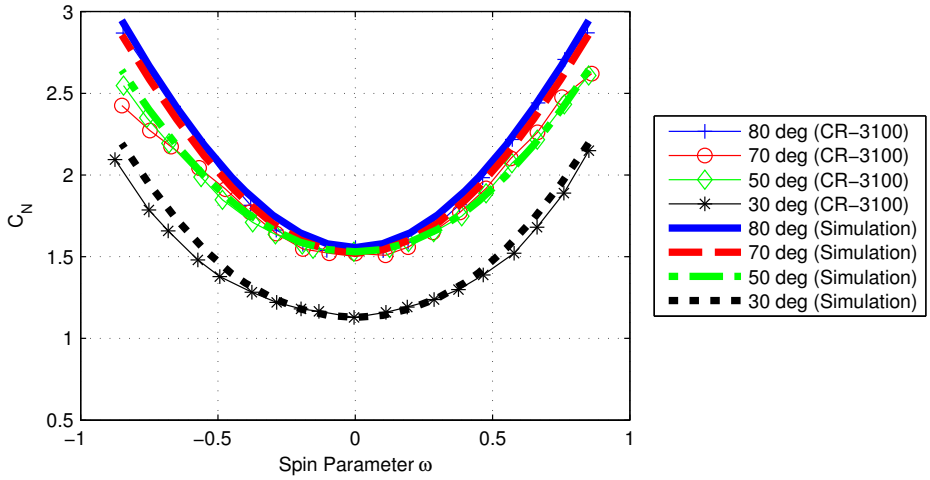

(b)

Figure 8. Plot of C_N versus ω for $R_s = 0$ at four analytically-modeled θ values compared to the rotary balance data of the low-wing general aviation full-airplane configurations of a) Ref. 43 with $\mathcal{AR} = 7.24$ and $\lambda = 0.67$, and b) Ref. 44 with $\mathcal{AR} = 5.9$ and $\lambda = 1$.

$$RMS = \sqrt{\frac{\sum_{i=1}^{n} (y_{i,exp} - y_{i,sim})^2}{n}} \tag{20}$$

where $y_{i,exp}$ is the experimental value for C_N, $y_{i,sim}$ is the analytically-modeled C_N value, and n is the number of data points in the compared datasets. Figure 9 presents comparisons of the RMS error averaged across ten experimental datasets and a strip-theory-based force calculator using Eq. 14, as derived in this paper to correct for rotational effects, as well as one using Eq. 4 of Ref. 13, the current state of the literature, to correct for rotational effects.

The first approach, labeled "Current Method," corrects the strip-theory-based force calculator with Eq. 14, the analytical methodology derived in this paper. The second approach, labeled "Ref. 13," corrects the force calculator with Eq. 4, which represents the current state of the literature. Figure 9 also compares the corrections of the current model and Ref. 13 for spin parameter values of $|\omega| > 0.5$. This regime is important because improving the fidelity of modeling the forces at high ω values can allow for the expansion of the range over which spins may be accurately modeled and hopefully reduce the regime over which full scale flight tests or dynamically-scaled spin tunnel tests must be performed.

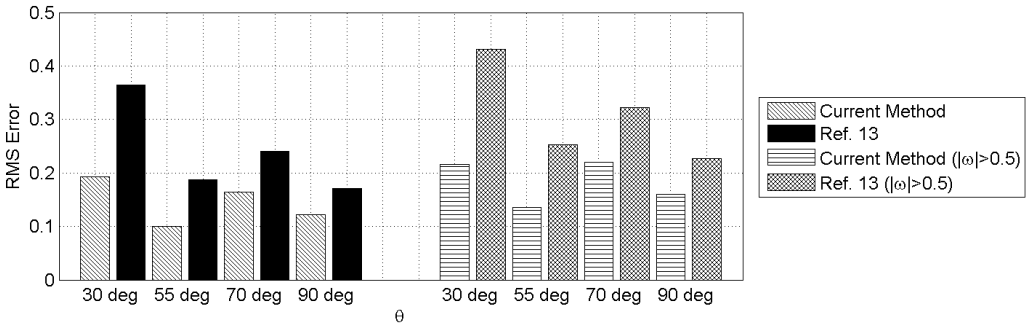

Figure 9. Average of RMS error values of the current method (Eq. 14) and Ref. 13 (Eq. 4) across ten experimental datasets.

As shown in Fig. 9, the current method of Eq. 14 has lower RMS error values than Ref. 13 at all four θ values studied over the full range of ω (left) and over the higher $|\omega| > 0.5$ regime (right). The largest improvement is demonstrated at $\theta = 30$ deg, with the advantage decreasing as θ increases towards 90 deg. It is noted that the RMS error values were the largest for $\theta = 30$ deg and lowest for $\theta = 55$ deg, with the RMS error values at 70 and 90 deg being the second highest and second lowest, respectively. This trend was repeated for the $|\omega| > 0.5$ regime, although the RMS error values for all cases were slightly higher in this regime than across the full $-1 < \omega < 1$ regime. This similar trend of the most accurate results occurring at 90 deg and the least accurate results at 30 deg for both models may be explained by the fact that both are based on the same general concept of centrifugal pumping, with the distinguishing conceptual difference being the tip ejection of fluid in the model of this paper. When broken down into individual datasets, the results of the current method had the lower RMS error value in 32 of 40 (four α values across 10 datasets) instances when compared to the method of Ref. 13. When the RMS error for $|\omega| > 0.5$ was calculated, the results of the current model once again were lower 32 times out of 40, many times by greater margins than over the full $-1 < \omega < 1$ regime.

The demonstration of lower RMS error values than the results of the method of Ref. 13 over the entire ω range shows that the results of the current method represent an improvement over previous research. Because the current method maintains an RMS error advantage at the higher values of $|\omega| > 0.5$, the authors suggest that this increased accuracy at larger ω values (more-extreme flight conditions) will allow the current model to expand the envelope of aircraft orientations that may be accurately modeled. It is hoped that this will allow certain stall/spin situations to be better simulated, and this ability may be incorporated into higher fidelity loss-of-control or unusual attitude simulators. A need for this increased level of simulator fidelity and "extended envelopes" has recently been mandated by the FAA.[12] Thus, this improved methodology, in addition to having the potential to satisfy newly-enacted simulator requirements, is hoped to have the potential to contribute to better pilot training for unusual-attitude flight in order to save lives.

Further research should shed light as to whether this model would be applicable to only general aviation-type aircraft, or if it may potentially show promise in the modeling of transport category aircraft, such as the Boeing 737 or Airbus A330. A potential for application of this methodology to analyses involving flapping-wing flight and hovering flight of micro air vehicles and insects may also exist, as it was demonstrated here that applying concepts developed from very low Reynolds number rotational experiments to the $Re \approx 100,000$ regime resulted in good agreement with experimental data. Because the model was validated against wind tunnel data over the range $3,000 < Re < 25,000$ and rotary balance data of $Re \approx 100,000$ yet based on concepts from very low Reynolds number studies, it seems plausible that the methodology may be applicable in the very low Reynolds number regime from which the general concepts were justified (i.e., MAV and insect flight studies). Future tunnel tests and work will hopefully shed some light as to the degree of applicability of this paper's proposed methodology to wings of significantly varying taper ratio λ.

VIII. Conclusions

A novel analytical method for modeling the increased force on a stalled wing due to radial pumping of the fluid in the stalled wake region is presented, and the model was validated against wind tunnel tests conducted specifically as part of this research. The model was then applied to simulating full-airplane configurations. This method, which advances the state of the field and improves upon the previous state of the literature, accounts for the increase in the

sectional C_d beyond 2 through the presence of 3D flow effects which act as a sink that entrains additional flow and increases the amount of freestream flow from which momentum is removed. The model was demonstrated to capture qualitative effects seen over a broad selection of experimental data, and offers better overall agreement than the current state of the literature. The assumptions and theory behind this model were demonstrated to correspond to the results and observations in the current literature in the fields of general aviation aircraft stall/spin, nonrotating spoiler or bluff body drag studies, and of flapping or rotating wing flight. The reason for differences between results from this model and horizontal axis wind turbine observations were addressed, and attributed to the very different $\mathcal{AR}$ values of general aviation wings and wind turbine blades.

It is hoped that, by offering a more-accurate first-principles based model, the ability to incorporate a better design-for-spin into the design of aircraft will be improved. While this model was developed for and validated against general aviation-type aircraft, it may prove easily adaptable to analyses involving flapping-wing and hovering flight of insects and micro air vehicles. This methodology also appears promising for increasing the simulation fidelity of flight simulators for transport category aircraft in stall and post-stall regions of the flight envelope, with an ultimate goal of saving lives and preventing accidents.

Acknowledgments

The authors would like to thank Robert W. Deters for sharing his knowledge and volunteering his help with the instrumentation setup for the wind tunnel tests, Gavin K. Ananda for his help in explaining and helping modify the LabVIEW code used for tunnel control and data acquisition, and Michael Rybalko for providing his insight and suggestions.

References

[1]Ragheb, A. M., Dantsker, O. D., and Selig, M. S., "Stall/Spin Flight Testing with a Subscale Aerobatic Aircraft," AIAA Paper 2013-2806, June 2013.

[2]Zimmerman, C. H., "Preliminary Tests in the NACA Free-Spinning Wind Tunnel," NACA Report 557, 1937.

[3]Soule, H. A. and Scudder, N. F., "A Method of Flight Measurement of Spins," NACA Report 377, 1931.

[4]Stephens, A. V., "Recent Research on Spinning," *Royal Aircraft Society Journal*, November 1933, pp. 944–955.

[5]AOPA Air Safety Foundation, "Joseph T. Nall Reports (1997-2010)," http://www.aopa.org/asf/publications/nall.html, Accessed January 2012.

[6]Hreha, M. A. and Lutze, F. H., "A Dynamic Model for Aircraft Poststall Departure," AIAA Paper 83-0367, 1983.

[7]Lutze, F. H. and Lluch, D., "Simulation of Stall, Spin, and Recovery of a General Aviation Aircraft," AIAA Paper 96-3409, 1996.

[8]Feistel, T. W. and Anderson, S. B., "Alleviation of Spin-Entry Tendencies through Localization of Wing-Flow Separation," *Journal of Aircraft*, Vol. 18, No. 2, 1981, pp. 69–75.

[9]Pamadi, B. N. and Taylor, L. W., "Estimation of Aerodynamic Forces and Moments on a Steadily Spinning Airplane," *Journal of Aircraft*, Vol. 21, No. 12, 1984, pp. 943–954.

[10]Polhamus, E. C., "Effect of Flow Incidence and Reynolds Number on Low-Speed Aerodynamic Characteristics of Several Noncircular Cylinders with Applications to Directional Stability and Spinning," NASA TN 4156, January 1958.

[11]Adams, W. M., "Analytic Prediction of Airplane Equilibrium Spin Characteristics," NASA Technical Paper TN D-6926, November 1972.

[12]Federal Aviation Administration, "14 CFR Part 60: Flight Simulation Training Device Qualification Standards for Extended Envelope and Adverse Weather Event Training Tasks; Proposed Rule," *Federal Register*, Vol. 179, No. 132, 2014.

[13]McCormick, B. W., "The Prediction of Normal Force and Rolling Moment Coefficients for a Spinning Wing," NASA Contractor Report CR-165680, February 1981.

[14]Bihrle, W., Hultberg, R. A., and Mulcay, W., "Rotary Balance Data for a Typical Single-Engine Low-Wing General Aviation Design for an Angle-of-Attack Range of 30 to 90 deg," NASA Contractor Report CR-2972, July 1978.

[15]Clarkson, M. H., Malcolm, G. N., and Chapman, G. T., "Experimental Determination of Post-Stall Rotary Derivatives for Airplane-Like Configurations at Several Reynolds Numbers," AIAA Paper 75-171, January 1975.

[16]Tischler, M. B. and Barlow, J. B., "Determination of the Spin and Recovery Characteristics of a General Aviation Design," *Journal of Aircraft*, Vol. 18, No. 4, 1981, pp. 238–244.

[17]Bihrle, W. and Barnhart, B., "Spin Prediction Techniques," *Journal of Aircraft*, Vol. 20, No. 2, 1983, pp. 97–101.

[18]Pamadi, B. N. and Taylor, L. W., "Semiempirical Method for Prediction of Aerodynamic Forces and Moments on a Steadily Spinning Light Airplane," NASA TM 4009, December 1987.

[19]Ragheb, M. and Ragheb, A. M., "Wind Turbines Theory - The Betz Equation and Optimal Rotor Tip Speed Ratio," *Fundamental and Advanced Topics in Wind Power*, edited by R. Carriveau, InTech, Rijeka, Croatia, 2011, pp. 19–38.

[20]Pomeroy, B. W. and Uhlig, D. V., "Boomerang Flight Tests," AIAA Paper 2014-3127, June 2014.

[21]Hoff, R. I. and Gratton, G. B., "Spin Induced Aerodynamic Flow Conditions on Full-Scale Aeroplane Wing and Horizontal Tail Surfaces," *Aeronautical Journal*, Vol. 117, No. 1198, 2013, pp. 1207–1231.

[22]Winkelmann, A. E. and Barlow, J. B., "Flowfield Model for a Rectangular Planform Wing beyond Stall," *AIAA Journal*, Vol. 18, No. 8, 1980, pp. 1006–1008.

[23]Weihs, D. and Katz, J., "Cellular Patterns in Poststall Flow over Unswept Wings," *AIAA Journal*, Vol. 21, No. 12, 1983, pp. 1757–1759.

[24]Broeren, A. P. and Bragg, M. B., "Spanwise Variation in the Unsteady Stalling Flowfields of Two-Dimensional Airfoil Models," *AIAA Journal*, Vol. 39, No. 9, 2001, pp. 1641–1651.

[25]Carr, Z., Chen, C., and Ringuette, M. J., "The Effect of Aspect Ratio on the Three-Dimensional Vortex Formation of Rotating Flat-Plate Wings," AIAA Paper 2013-0912, January 2012.

[26]Arie, M. and Rouse, H., "Experiments on Two-Dimensional Flow Over a Normal Wall," *Journal of Fluid Mechanics*, Vol. 1, No. 2, 1956, pp. 129–141.

[27]Garmann, D. J. and Visbal, M. R., "Dynamics of Revolving Wings for Various Aspect Ratios," *Journal of Fluid Mechanics*, Vol. 748, 2014, pp. 932–956.

[28]Garmann, D. J., Visbal, M. R., and Orkwis, P. D., "Three Dimensional Flow Structure and Aerodynamic Loading on a Revolving Wing," *Physics of Fluids*, Vol. 25, No. 3, 2013, 034101.

[29]Bross, M., Ozen, C. A., and Rockwell, D., "Flow Structure on a Rotating Wing: Effect of Steady Incident Flow," *Physics of Fluids*, Vol. 25, No. 8, 2013, 081901.

[30]Hu, D., Hua, O., and Du, Z., "A Study on Stall-Delay for Horizontal Axis Wind Turbine," *Renewable Energy*, Vol. 31, No. 6, 2005, pp. 821–836.

[31]Lindenburg, C., "Modelling of Rotational Augmentation Based on Engineering Considerations and Measurements," *Energy Research Center of the Netherlands, Petten, ECN-RX-04-131, November 2004, Presented at the European Wind Energy Conference, London, England*, December 2000.

[32]Himmelskamp, H., "Profile Investigations of a Rotating Airscrew," Ph.D. Thesis, Gottingen, 1945, MAP Volkenrode Reports and Translation No. 832, 1947.

[33]Jamieson, P., *Innovation in Wind Turbine Design*, John Wiley & Sons, New York, NY, 2011.

[34]Jonkman, J., Butterfield, S., Musial, W., and Scott, G., "Definition of a 5-MW Reference Wind Turbine for Offshore System Development," National Renewable Energy Laboratory Technical Report NREL/TP-500-38060, February 2009.

[35]Fail, R., Lawford, J. A., and Eyre, R. C. W., "Low-Speed Experiments on the Wake Characteristics of Flat Plates normal to an Air Stream," Aeronautical Research Council Reports and Memoranda 3120, 1959.

[36]Tangler, J. L. and Selig, M. S., "An Evaluation of an Empirical Model for Stall Delay due to Rotation for HAWTS," *National Renewable Energy Laborator, Golden, CO, NREL/CP-440-23258, Presented at Windpower '97, Austin, TX*, June 1997.

[37]Fage, A. and Johansen, F. C., "On the Flow of Air Behind an Inclined Flat Plate of Infinite Span," *Proc. R. Soc. Lond.*, Vol. 116, No. 773, 1927, pp. 170–197.

[38]Selig, M. S., "Real-Time Flight Simulation of Highly Maneuverable UAVs," *Journal of Aircraft*, AIAA Early Edition, doi: 10.2514/1.C032370, 2014, pp. 1–21.

[39]Khodadoust, A., "An Experimental Study of the Flowfield on a Semispan Rectangular Wing with a Simulated Glaze Ice Accretion," Ph.D. Thesis, Department of Aeronautical and Astronautical Engineering, University of Illinois at Urbana-Champaign, Urbana, IL, 1993.

[40]Selig, M. S. and McGranahan, B. D., "Wind Tunnel Aerodynamic Tests of Six Airfoils for Use on Small Wind Turbines," National Renewable Energy Laboratory Subcontractor Report NREL/SR-500-34515, October 2004.

[41]Brandt, J. B., "Small-Scale Propeller Performance at Low Speeds," M.S. Thesis, Department of Aerospace Engineering, University of Illinois at Urbana-Champaign, Urbana, IL, 2005.

[42]Deters, R., "Performance and Slipstream Characteristics of Small-Scale Propellers at Low Reynolds Numbers," Ph.D. Thesis, Department of Aerospace Engineering, University of Illinois at Urbana-Champaign, Urbana, IL, 2014.

[43]Ralston, J. N., "Rotary Balance Data for a Typical Single-Engine General Aviation Design for an Angle-of-Attack Range of 8 to 90 deg: I - Influence of Airplane Components for Model D," NASA Contractor Report CR-3246, March 1983.

[44]Hultberg, R. S. and Mulcay, W., "Rotary Balance Data for a Typical Single-Engine General Aviation Design for an Angle-of-Attack Range of 8 to 90 deg: I - Low-Wing Model A," NASA Contractor Report CR-3100, February 1980.